Supplementary Material for "**Parity-Dependent Moiré Superlattices in Graphene/*h*-BN Heterostructures: A Route to Mechanomutable Metamaterials**"

Wengen Ouyang[1], Oded Hod[2*], and Michael Urbakh[2]

[1]*Department of Engineering Mechanics, School of Civil Engineering, Wuhan University, Wuhan, Hubei 430072, China*
[2]*Department of Physical Chemistry, School of Chemistry and The Sackler Center for Computational Molecular and Materials Science, The Raymond and Beverly Sackler Faculty of Exact Sciences, Tel Aviv University, Tel Aviv 6997801, Israel.*

Email: odedhod@tauex.tau.ac.il

This supplementary material file contains the following sections:

1 Methodology

1.1 Model system

To build the periodic alternating graphene/*h*-BN heterostructures while preserving the small experimental lattice mismatch (~1.8%) between graphene and *h*-BN, we followed the method outlined in Refs. [1,2] and built large rectangular supercells, where each graphene and *h*-BN layer contains 12,544 and 12,120 atoms, respectively. We considered two types of heterostructures with different periodic boundary conditions. One type, in which periodic boundary conditions are applied along the lateral directions alone is termed 2D PBC and the other type, where periodic boundary conditions are applied along the vertical direction as well is termed 3D PBC. Note that for the 3D PBC systems we tested two supercell thicknesses to verify the convergence of our results with respect to inter-image interactions. The Open Visualization Tool (Ovito) was used to visualize atomic configurations [3].

1.2 Force fields

Intralayer interactions for graphene and *h*-BN layers are modeled using the second generation REBO potential [4] and the Tersoff potential [5], respectively. Interlayer interactions are modeled using the registry-dependent interlayer potential ILP [6,7], which were recently reparametrized to better describe the sub-equilibrium regime for bilayer [8] and bulk configuration [9], respectively. The former and latter parametrizations are used for bilayer and multilayer graphene/*h*-BN heterostructures, respectively. We checked that using the latter parametrization for the bilayer configuration gives equivalent results, with a slightly reduced out-of-plane corrugation (8.54 Å vs. 8.6 Å). We further checked that increasing the ILP cutoff parameter from 16 Å to 24 Å does not influence our results.

1.3 Simulation setup for energy minimization

All geometry optimization simulations were performed with the LAMMPS simulation package [10]. The alternating graphene/*h*-BN heterostructures with various number of layers are first heated up to 1000 K and then cooled down to 300 K during 100,000 steps using the Nosé-Hoover thermostat with a time-step of 0.25 fs, followed by thermal equilibration at 300 K and zero pressure for another 100,000 steps with a time-step of 0.5 fs, where the pressure is controlled by the Nosé-Hoover barostat [11]. After annealing, the configurations are optimized by fixing the size of the simulation box using the FIRE algorithm [12] with a force convergence criterion of 10^{-5} eV/Å and a time-step of 1 fs. Once reaching the local minimum, the conjugate gradient (CG) method is used to relax the simulation box with a force convergence criterion of 10^{-3} eV/Å. To fully relax the system, the above procedure (FIRE + CG) is repeated for ten times and followed by a final optimization with FIRE algorithm with a force convergence criterion of 10^{-5} eV/Å (convergence tests for this procedure are provided in Sec. 3.2 of the supplementary material). To verify that our results are not influenced by the lateral dimensions of the supercell we doubled the simulation box along the *x*-direction (see Sec. 3.1) and repeated the optimization procedures. The results of these tests yielded the same optimized configurations thus confirming that our supercell is sufficiently large to describe studied superstructures.

We note that two other minimization protocols were considered (see details in Sec. 2), where the size of the simulation box was kept fixed and the geometry optimization was performed with or without annealing. Comparing the results of the three protocols we conclude that cycles of annealing the system and relaxing the simulation box are important to avoid trapping in local minima (see Fig. S1 and Fig. S2) and that in-plane stresses play an important role for the resulting superstructures.

1.4 Simulation Protocol for calculating Poisson's ratio and Young's modulus

To calculate Poisson's ratio of the graphene/*h*-BN heterostructures, we applied strain (ϵ_x ranging from -0.003 to 0.003) to the structures along the *x*-direction of the box (see Fig. 1 in the main text) and the translational vectors (L_y) of the simulation cell in the *y*-direction was relaxed at zero pressure by a Nosé-Hoover barostat with a time constant of 1.0 ps for the lattice vectors relaxation [11]. The system temperature was controlled via a Nosé-Hoover thermostat, which was set to 5 K and 300 K in our simulations as detailed in the main text. The time step used in these simulations was set to 0.5 fs. The strain in the relaxed directions was then calculated using $\epsilon_y = \left(L_y - L_y^0\right)/L_y^0$, where L_y^0 is the equilibrium size of the simulations cell in the *y* direction at the desired temperature. Poisson's ratio is then calculated as $\mu_{xy} = -\epsilon_y/\epsilon_x$. By measuring the average stress (σ_x) along *x*-direction during the simulations, the Young's modulus of the alternating graphene/*h*-BN heterostructures was extracted from the linear regime of the σ_x versus ϵ_x curve.

2 Comparison of Minimization Protocols

2.1 Effect of annealing and relaxing the simulation box

To test the viability of the obtained optimized structure, three different energy minimization protocols were considered: (i) the structure was minimized without annealing and the size of the simulation box was kept fixed; (ii) the structure was annealed (first heating the system to 1000 K then gradually cooling it down to 300 K) before minimization and the size of the simulation box was kept fixed; and (iii) the structure was annealed as in (ii) and the size of the simulation box was relaxed during annealing and energy minimization processes. To demonstrate the importance of annealing and relaxing the simulation box during energy minimization, we first optimized the bilayer and trilayer graphene/*h*-BN heterostructures with the abovementioned protocols. For the bilayer case, protocols (i) and (ii) gave the same optimized structure with a well-defined moiré pattern and an out-of-plane corrugation (peak-to-deep value) of ~5.3 Å [see Fig. S1(a)], which is consistent with previous results [2,6]. Protocol (iii) resulted in a similar moiré pattern [see Fig. S1(b)], but with a considerably larger surface corrugation of ~8.6 Å. The reason is that protocols (i) and (ii) produce in-plane tensile stress (~0.15 GPa) that reduces the out-of-plane corrugation. Allowing for box relaxation the lateral dimensions contract by ~0.6%, resulting in a release of the in-plane tensile stress and a corresponding enhancement of the out-of-plane corrugation. The total energies of the optimized structures using protocols (i) and (ii) were -184,203 and -184,219 eV/supercell, respectively, for a supercell consisting of 24,644 atoms. For the trilayer graphene/*h*-BN heterostructure, the optimized structure from protocols (i) and (ii) exhibited hexagonal and trigonal superstructures with out-of-plane corrugation of ~0.2 Å and ~5.3 Å and total energies of -275,650 and -275,672 eV/supercell, respectively, for a supercell consisting of 36,744 atoms (a-b), which is double the size of the minimal supercell required to obtain the relevant superstructures. Notably, protocol (iii) resulted in the highly corrugated (~13 Å) flamingo pattern with a lower potential energy of -275,696 eV/supercell, as discussed in the main text [Fig. 1(c) in the main text, also presented in Fig. S2(c)].

From these results it is clearly evident that the annealing procedure is important to identify local minima on the complex superstructure energy surface characterizing the studied systems. Furthermore, we find that in-plane stress can influence the obtained superstructure. Since we are interested herein in unstressed systems, we adopted protocol (iii) for all calculations presented in the main text. We note that future work on the effect of stress on the superstructure of layered heterostructures is being pursued.

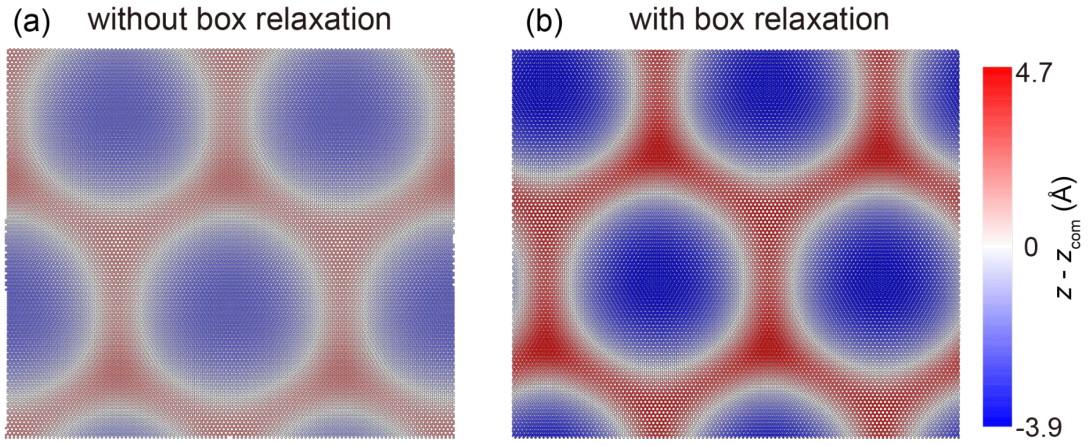

FIG. S1. Effect of box relaxation on the energy minimization of a bilayer graphene/*h*-BN heterostructure. Panels (a) and (b) correspond to the optimized structure without and with box relaxation, respectively. The color scale denotes the height of the top layer atoms with respect to its center-of-mass. To show the difference clearly, the same color scale is used in both panels. The full double-sized supercell that was used to perform these calculations is presented.

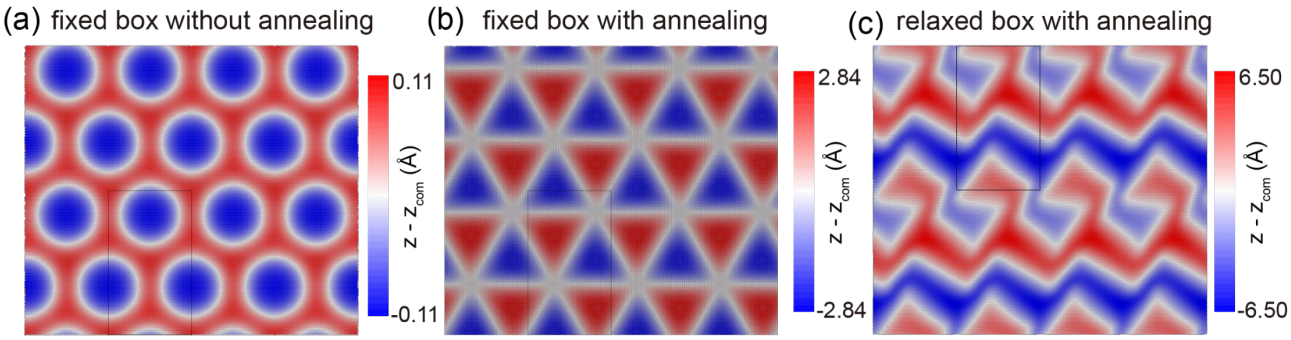

FIG. S2. Effect of box relaxation and annealing on the energy minimization of a trilayer alternating graphene/h-BN heterostructure. Panels (a) and (b) correspond to the fixed box dimensions optimized structure without and with annealing (protocols i and ii), respectively. Panel (c) shows the optimized structure with both annealing and box relaxation (protocol iii, same as Fig. 2 in the main text). The color scale denotes the height of the top layer atoms with respect to its center-of-mass. The modeled supercell is marked by the black rectangle in each panel.

2.2 Relative Stability of the Optimized Trilayer Graphene/h-BN Superstructures

To check the stability of the different trilayer graphene/*h*-BN heterostructures illustrated in Fig. S2, we performed nudged elastic band (NEB) simulations [13,14] to calculate the energy barrier to transform between them. Since the NEB method implemented in LAMMPS is implemented with fixed box size, we could only calculate the energy barrier between the states illustrated in Fig. S2(a) and Fig. S2(b) that have the same box dimensions. Fig. S3 shows the results of the NEB calculations, where the total potential energy is plotted along the reaction coordinate (r) from the state with triangle pattern [Fig. S2(b), $r = 0$] to the state with hexagonal pattern [Fig. S2(a), $r = 1$]. The fact that there is no barrier near $r = 1$ indicates that the hexagonal superstructure is either a saddle point or a very shallow local minimum on the potential energy surface (the estimated barrier is smaller than 8.62×10^{-3} meV/supercell). The energy difference between the two states is ~21.7 eV/supercell, for a supercell size consisting of 36,744 atoms. We further note that there exists an equivalent mirror-image structure of the triangular pattern. The small barrier of ~0.43 eV/supercell [see Fig. S3(b)] separating

them indicates that the two states can co-exist at room temperature. Finally, to evaluate the stability of the Flamingo superstructure we performed room temperature molecular dynamic simulations for the structure appearing in Fig. S2(c), showing that the structure is stable over a simulation time of at least 200 ps (see Supplementary Movie 1) with no signatures of degradation.

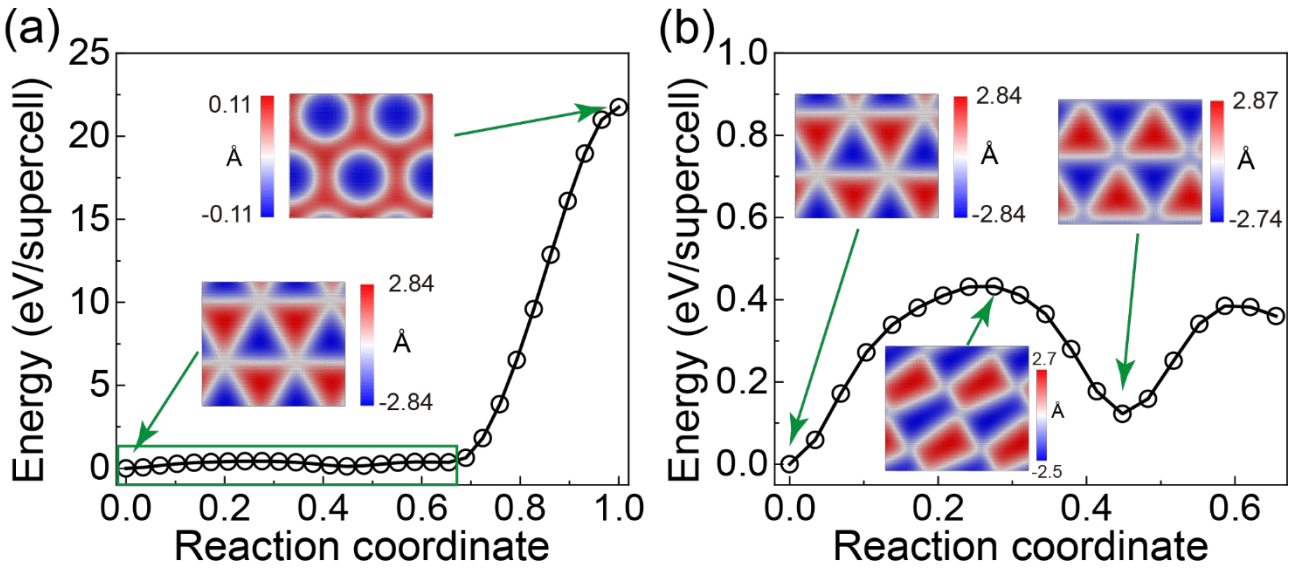

FIG. S3. NEB calculations for a trilayer graphene/*h*-BN heterostructure with a rectangular supercell of 13.77 nm × 23.86 nm, which contains 36,744 atoms. (a) Total potential energy along the reaction coordinate from the triangular state (b) to the hexagonal state [Fig. S2(a)]. The lowest energy state is shifted to zero for clarity of the presentation. (b) Total potential energy along the reaction coordinate for the zoomed-in region marked by the green rectangle in panel (a) showing the transition pathway between two mirror-image triangular superstructures. Representative snapshots are chosen to show the local minima and transition state structures along the reaction coordinate. The color scale denotes the height of the top layer atoms with respect to its center-of-mass.

2.3 Stability of the alternating graphene/h-BN heterostructures

To check the stability of the alternating graphene/*h*-BN heterostructures with various number of layers, we calculated the energy per atom (relative to a single graphene layer), as a function of the number of layers, as illustrated in Fig. S4(a). Here, ΔE is defined as:

$$\Delta E(N) = \frac{E_{\mathrm{tot}}^{\mathrm{opt}}(N)}{N_{\mathrm{tot}}} - \frac{E_{\mathrm{Gr}}^{\mathrm{opt}}}{N_{\mathrm{Gr}}}, \tag{S1}$$

where $E_{\mathrm{tot}}^{\mathrm{opt}}(N)$ and $E_{\mathrm{Gr}}^{\mathrm{opt}}$ are the total energy of the optimized *N*-layer alternating graphene/*h*-BN heterostructures and isolated single layer graphene (with the same lateral size), respectively, and N_{tot} and N_{Gr} are the total number of atoms in the corresponding systems. As can be seen from the red points in Fig. S4(a), there is a clear parity dependence of $\Delta E(N)$, where the odd-numbered systems show lower energy than their even-numbered counterparts. The negative values of ΔE in the whole range of *N* indicates the relative stabilities of the regular moiré and flamingo heterostructures compared to a single graphene layer. This is to be expected due to the interlayer attraction at the corresponding interlayer distances (see Fig. S4 (b)). Notably, the bulk configurations (3D PBC) have very close energy with that of the odd-numbered systems.

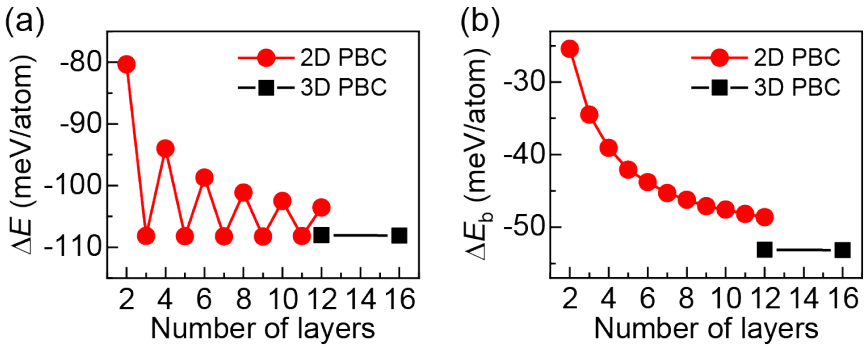

FIG. S4. (a) Energy of alternating graphene/*h*-BN heterostructures calculated with respect to a single layer graphene as a function of the number of layers. (b) Effective binding energy of alternating graphene/*h*-BN heterostructures with different number of layers. The red circles and black squares correspond to the 2D PBC and 3D PBC results, respectively.

To further support this conclusion, we also calculated the effective binding energy for the alternating graphene/*h*-BN heterostructures, which is defined as:

$$\Delta E_{\mathrm{b}}(N) = \frac{E_{\mathrm{tot}}^{\mathrm{opt}}(N=m+n) - nE_{\mathrm{Gr}}^{\mathrm{opt}} - mE_{h\mathrm{BN}}^{\mathrm{opt}}}{N_{\mathrm{tot}}}, \quad \text{(S2)}$$

where $E_{h\mathrm{BN}}^{\mathrm{opt}}$ is the total energy of an optimized isolated single *h*-BN layer (with the same lateral size of the corresponding heterostructures), and *n* and *m* are the number of layers of graphene and *h*-BN in the heterostructures, respectively. The results of ΔE_{b} as a function of *N* are presented in Fig. S4 (b), where a monotonic increase in the binding energy (in absolute value) with increasing *N* is observed and the 2D PBC results are approaching the 3D PBC results (53.18 meV/atom), which can be considered as the bulk limit.

These results indicate that both the regular moiré and flamingo heterostructures patterns are (meta-)stable and are expected to be found in experiment.

2.4 Relative stability of the heterostructures with flamingo and regular moiré patterns

To understand the crossover behavior of the parity dependence at a stack thickness of 7 layer, we performed a detailed comparison of the relative stability of the flamingo and regular moiré superstructures as a function of stack thickness.

To evaluate the relative stability for heterogeneous stacks including less than 8 layers, we had to identify odd heterogeneous stacks with regular moiré superstructures and even heterostructures with flamingo patterns. Above a thickness of 7 layers we had to identify regular moiré superstructures for all parities.

To obtain regular moiré superstructures for odd-systems below 8 layers and for all system above 7 layers (where the flamingo pattern is found to be more stable) we followed the following procedure. We first took the 6-layer fully optimized heterostructure with regular moiré patterns and duplicated it along the vertical (*z*) direction to generate a 12-layered stack. We then reoptimized this stack while fixing the supercell box dimensions. Then we removed 0-9 layers of the newly optimized 12-layer stack to obtain 12-3-layered stacks with regular moiré superstructures. These were then optimized with fixed box dimensions, yielding relaxed 3-, 5-, 7-, 8-, 9-, 10-, 11-, and 12-layered stacks with regular moiré superstructures.

To get flamingo patterns for even-numbered heterostructures with 2, 4 and 6-layers stack (where the regular moiré superstructures are more stable) we removed the top layer from the optimized flamingo structure obtained for odd-numbered systems with 3, 5 and 7-layer stack, respectively. The resulting stacks were then optimized with fixed box dimensions yielding meta-stable even-numbered flamingo

shaped stacks.

Figure S5(a) presents the energy difference between the flamingo and moiré superstructures as a function of the number of layers, $\Delta E(N) = E_{\text{flamigo}}(N) - E_{\text{moiré}}(N)$, showing that below a thickness of 7 layers, the flamingo superstructures are less (more) stable than the moiré counterparts for even (odd) systems, whereas above 7 layers the flamingo patterns are found to be more stable (negative $\Delta E(N)$) regardless of parity, demonstrating the crossover point mentioned by the referee.

As demonstrated in Fig. S5, the energy difference, $\Delta E(N)$, of the odd-layered systems scales linearly with the number of layers, whereas linear scaling in the even-layered stacks commences only after the crossover to flamingo patterns is obtained.

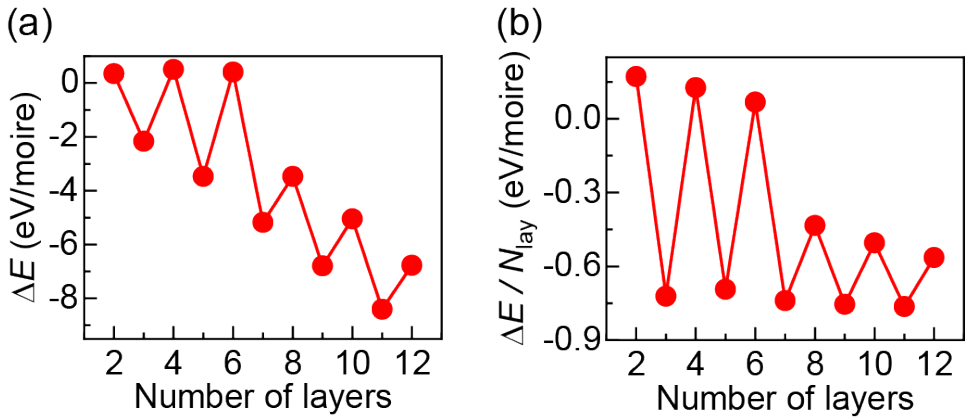

FIG. S5. The energy difference between moiré and flamingo superstructures as a function of the number of layers. (a) Energy difference per moiré supercell. (b) Energy difference per moiré supercell normalized by the number of layers. Note that we present the results in terms of energy per moiré supercell since the discussed effect is of collective nature.

3 Convergence tests

3.1 Convergence with Respect to Supercell Lateral Dimensions

The supercell lateral dimensions used to obtain the results presented in the main text are 13.77 nm × 23.86 nm. To verify convergence with respect to these dimensions, we repeated our calculations for several stack thicknesses with a larger supercell size of 27.54 nm × 23.86 nm. As shown in Fig. S6, the deformation pattern of the optimized heterostructures with increased supercell size are the same as those presented in the main text, indicating that the supercell dimensions adopted in the main text are sufficiently large to obtain consistent results.

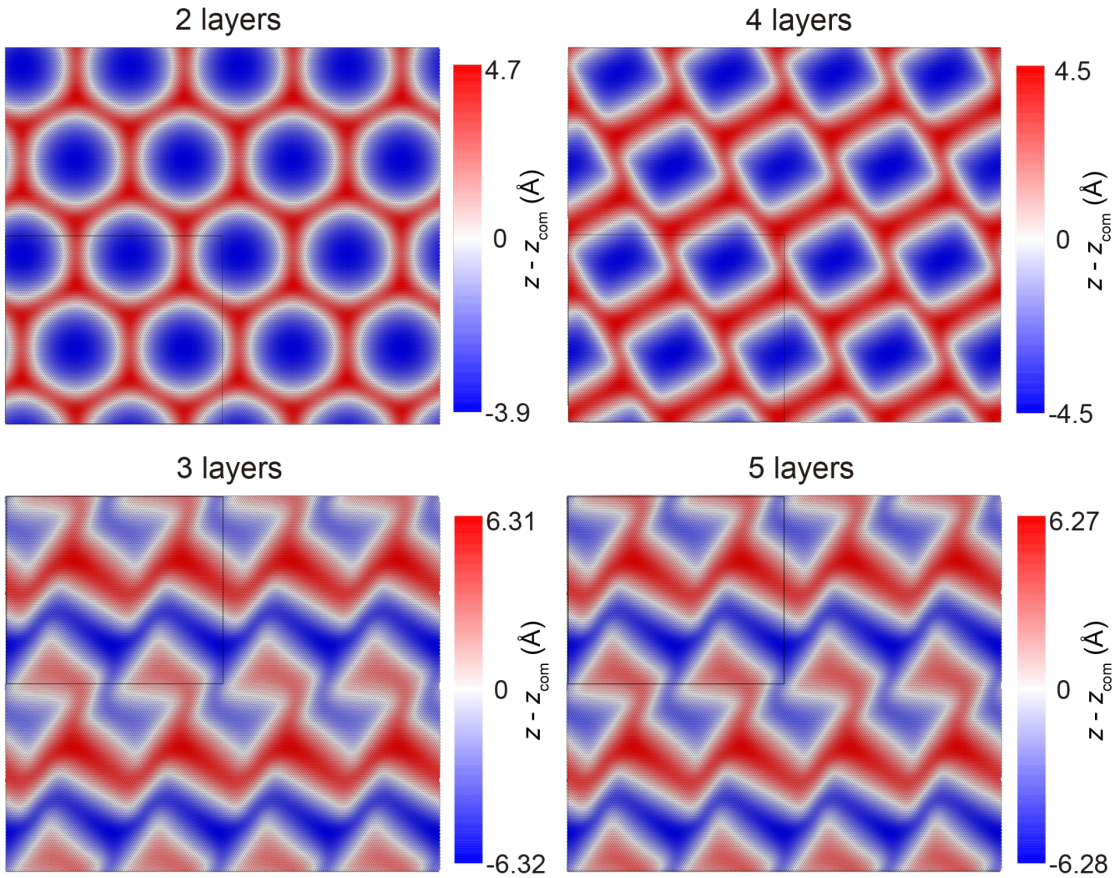

FIG. S6. Size Effect. Optimized structure for alternating graphene/*h*-BN heterostructures of lateral dimension of 27.54 nm × 23.86 nm and stack thicknesses ranging from 2 to 5 layers. The color scales denote the height of the top layer atoms with respect to its center-of-mass in each system. The modeled supercell is marked by the black rectangle in each panel.

3.2 Convergence with Respect to the Number of Optimization Cycles

As mentioned in the Methods section, the optimization procedure consisted of repeated cycles of geometry optimization with fixed simulation box dimensions using the FIRE algorithm followed by optimization of the supercell dimensions using the conjugate gradients method. To obtain the results presented in the main text, ten such cycles have been applied. In Fig. S7 we present typical convergence curves of the potential energy of the system, the size of the simulation box, and the in-plane stress with respect to the number of optimization cycles. The energy, supercell dimensions, and in plane stress considered converge after 6 optimization cycles to within 7×10^{-6} eV, 6×10^{-6} nm, and 2×10^{-6} GPa respectively, indicating that the results presented in the main text are well optimized.

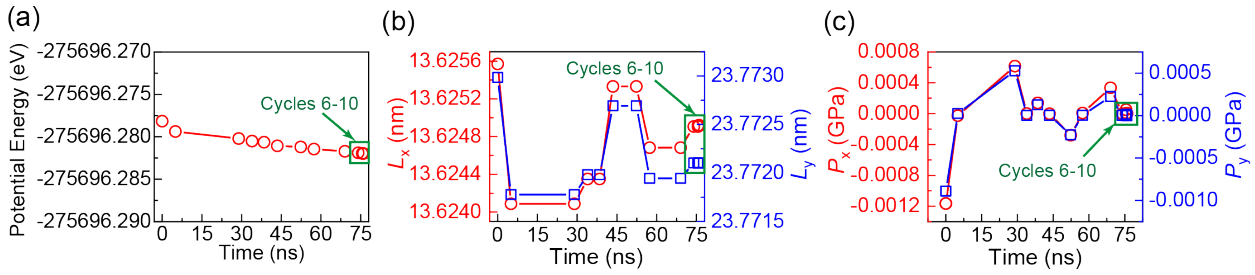

FIG. S7. Convergence test with respect to the number of optimization cycles for the trilayer graphene/*h*-BN heterostructure. Evolution of the (a) potential energy, (b) simulation box dimensions and (c) in-plane stress during the optimization cycles described in the Method section. The points inside the green rectangle belong to optimization cycles 6-10. The left and right axes in (b) and (c) represent the size of the simulation box and the in-plane stress of the system along *x* (open red cycles) and *y* (open blue rectangles) directions, respectively.

4 Additional Optimized Heterostructures

4.1 Optimized Heterostructures for Stack Thicknesses Exceeding 9 Layers

For brevity, we opted to present in the main text superstructures of alternating graphene/*h*-BN heterostructures with up to 9 layers. Here, we show results for thicker stacks of up to 16 layers. The results presented in Fig. S8 further support our conclusion made in the main text that alternating graphene/*h*-BN heterostructures with more than 7 layers present the Flamingo superstructure with no parity effect.

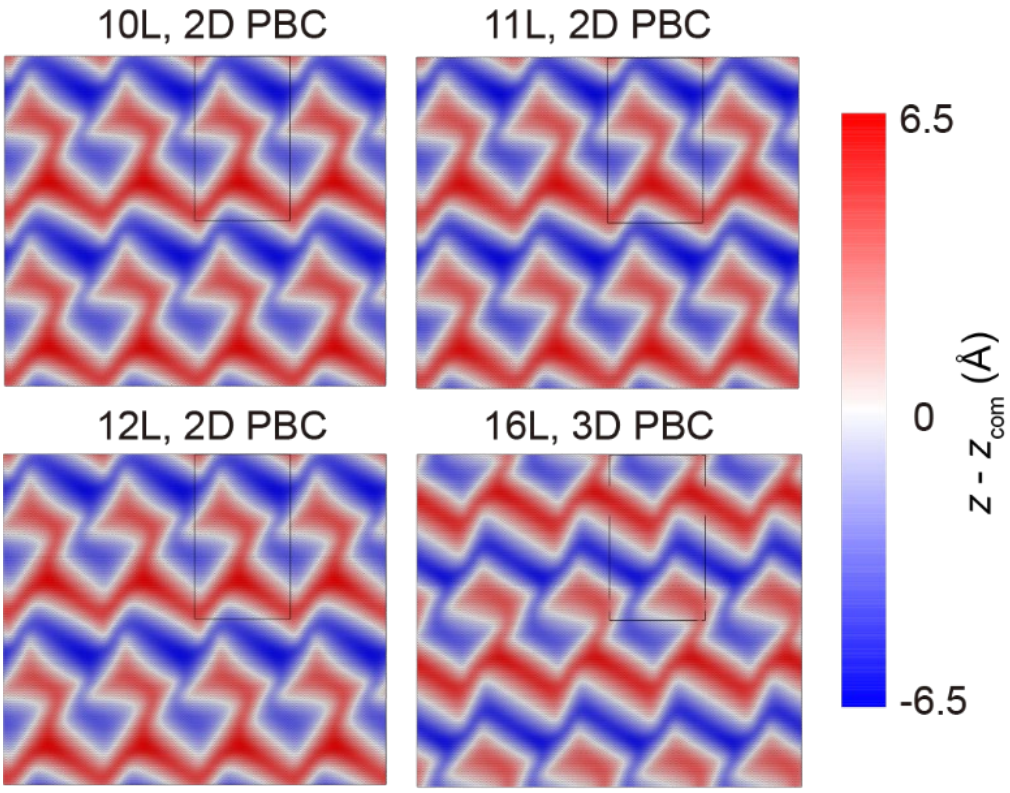

FIG. S8. The deformation pattern for alternating graphene/*h*-BN heterostructures with number of layers ranging from 10 to 16. To show the deformation pattern clearly, the simulation box (marked by black rectangle in each panel) is multiplicated along the lateral directions. The color scale denotes the atomic height with respect to the center-of-mass of the top layer.

4.2 Optimized Heterostructures with an Excess Graphene Layer

All odd-numbered stacks considered in the main text included an excess *h*-BN layer over graphene. For instance, the stacking of a 3-layer heterostructure was *h*-BN/graphene/*h*-BN. To consider the complementary stacks, we performed geometry optimization for alternating graphene/*h*-BN heterostructures with an excess graphene layer over *h*-BN. The flamingo patterns were found to be the energy favorable configurations for all four (N = 3, 5, 7, 9) odd-layered systems considered (see Fig. S9). These results thus further support the robustness of our findings regarding the stability of the flamingo patterns.

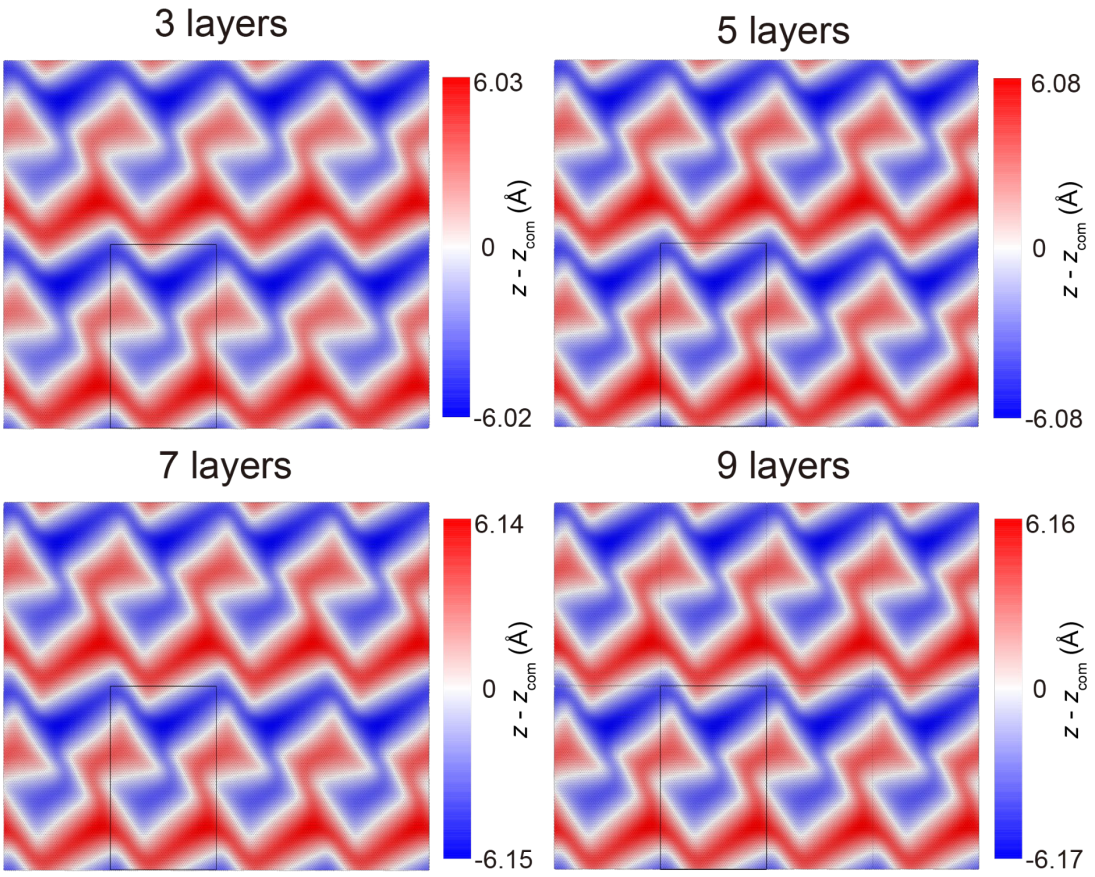

FIG. S9. The deformation pattern for odd alternating graphene/*h*-BN heterostructures (N = 3, 5, 7, 9) with an excess graphene layer. To show the deformation pattern clearly, the simulation box (marked by a black rectangle in each panel) is multiplicated along the lateral directions. The color scale denotes the atomic height with respect to the center-of-mass of the top layer.

5 Raw Data for Calculating Young's Modulus and Poisson's Ratio

In the main text we presented the calculated Young's modulus and Poisson's ratio for the various systems considered. For completeness, the raw data used to extract the values reported in the main text is provided herein for temperatures of 5 K and 300 K. Figs. S10 and S11 show the stress-strain relation along the *x*-direction for alternating graphene/*h*-BN heterostructures with the number of layers varying from 2 to 12 at 5 K and 300 K, respectively. The linear nature of these curves (linear fitting marked by the blue lines) indicates that the system is in the elastic regime and the slope of the stress-strain curve gives the Young's modulus of the heterostructures, which is listed in each panel of Figs. S10 and S11. It is clear that the parity dependence of the Young's modulus on the number of layers is not affected by temperature although its value slightly changes. The larger error bars appearing in Fig. S11 result from thermal fluctuations. Note that the heterostructures with 2 and 4 layers buckle at a compression strain of -0.2% at room temperature.

To calculate Poisson's ratio of the heterostructures, we applied strain along the *x*-direction and measured the corresponding variation of the simulation box size along the *y*-direction. Fig. S12 and Fig. S13 present the results obtained at 5 K and 300 K, respectively. As mentioned in the main text, the behavior of Poisson's ratio at room temperature is similar to that obtained at 5 K with a slight shift toward negative values, which may be attributed to the thermal expansion of the system with increasing temperature (see Fig. S14).

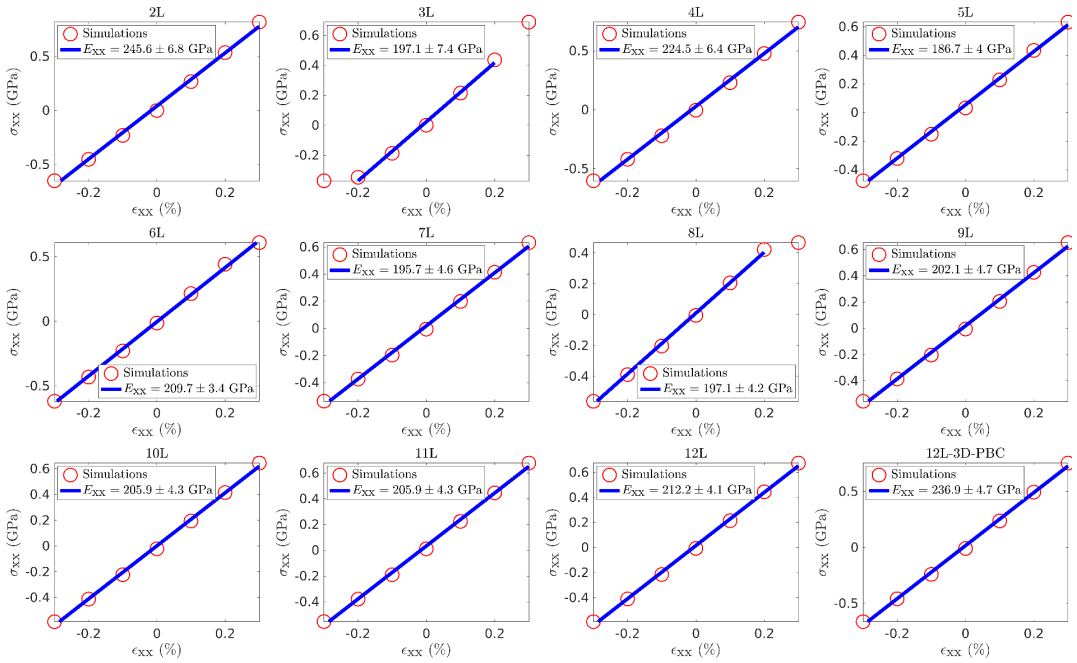

FIG. S10. Stress-strain curves obtained at a temperature of 5 K for alternating graphene/*h*-BN heterostructures with number of layers ranging from 2 to 12. The lower right panel provides results obtained using three-dimensional periodic boundary conditions.

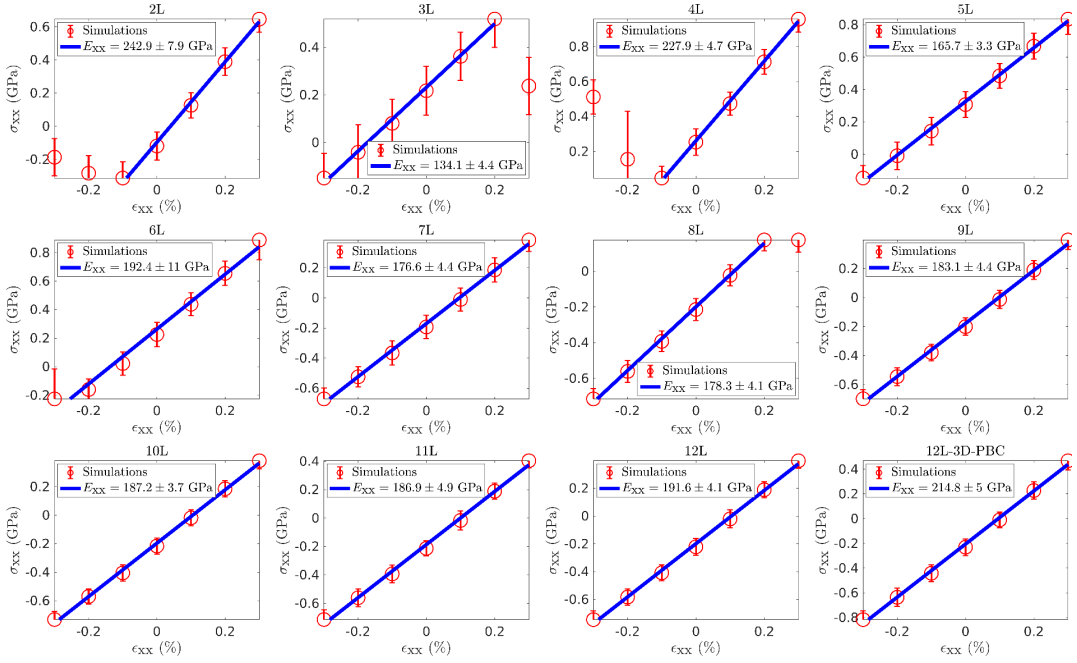

FIG. S11. Stress-strain curves obtained at a temperature of 300 K for alternating graphene/*h*-BN heterostructures with number of layers ranging from 2 to 12. The lower right panel provides results obtained using three-dimensional periodic boundary conditions.

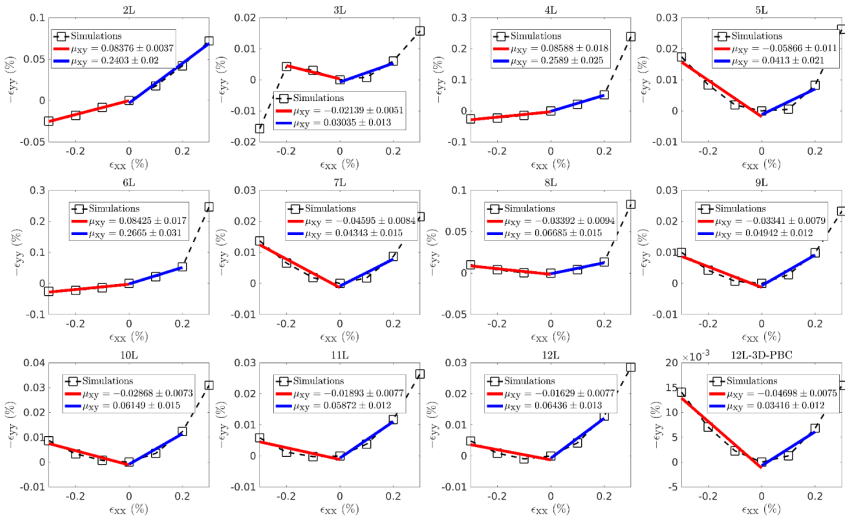

FIG. S12. Strain along the *y*-direction (ϵ_{yy}) as a function of the applied strain along *x*-direction calculated at a temperature of 5 K for alternating graphene/*h*-BN heterostructures with the number of layers varying from 2 to 12. The lower right panel provides results obtained using three-dimensional periodic boundary conditions. The sign of ϵ_{yy} is inverted such that the sign of the calculated Poisson's ratio will match the slope of the curve.

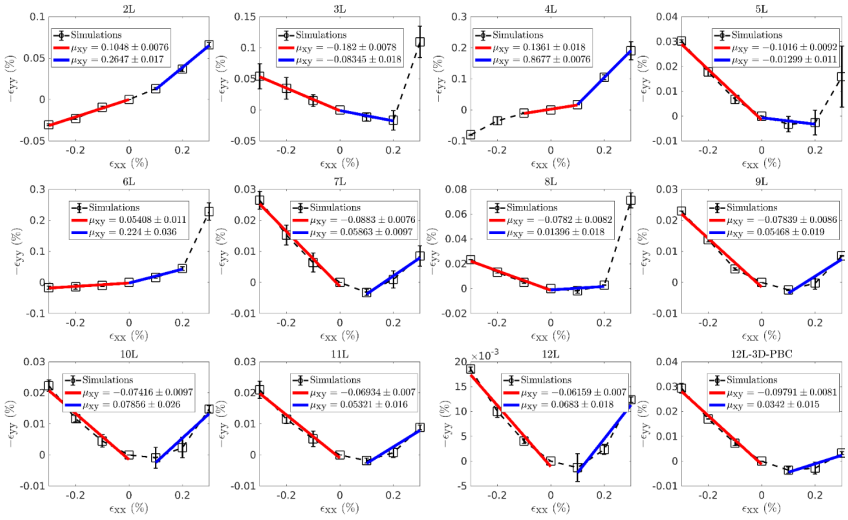

FIG. S13. Strain along the *y*-direction (ϵ_{yy}) as a function of the applied strain along *x*-direction calculated at a temperature of 300 K for alternating graphene/*h*-BN heterostructures with the number of layers varying from 2 to 12. The lower right panel provides results obtained using three-dimensional periodic boundary conditions. The sign of ϵ_{yy} is inverted such that the sign of the calculated Poisson's ratio will match the slope of the curve.

6 Thermal Expansion of Bulk Graphene/*h*-BN Heterostructures

In this section we demonstrate the thermal expansion effect of alternating bulk graphene/*h*-BN heterostructures. To study the thermal effect along each direction, a bulk configuration (12 layers with three-dimensional periodic boundary conditions) is used, the system is equilibrated with an NPT ensemble at a desired temperature (T_{set}) for 200 ps. The thermal strain is then evaluated by averaging over the following 100 ps. As shown in Fig. S14, the thermal strain along the *x*, *y* (lateral) and *z* (vertical) directions (see Fig. 1 in the main text) increases linearly with temperature. The slope of the curve gives the thermal expansion coefficient, which is $3.2671 \times 10^{-6}\ \mathrm{K}^{-1}$, $2.5381 \times 10^{-6}\ \mathrm{K}^{-1}$ and $3.9237 \times 10^{-5}\ \mathrm{K}^{-1}$ along the *x*, *y* and *z* directions, respectively. From Fig. S14 we can see that the thermal strain along the vertical direction [Fig. S14(c)] is an order of magnitude larger than that along the lateral directions [Fig. S14(a)-(b)], as expected for a van der Waals layered structure. Notably, the out-of-plane deformation corrugation remains nearly unaffected at the range of temperatures and simulation times considered [see Fig. S14(d)].

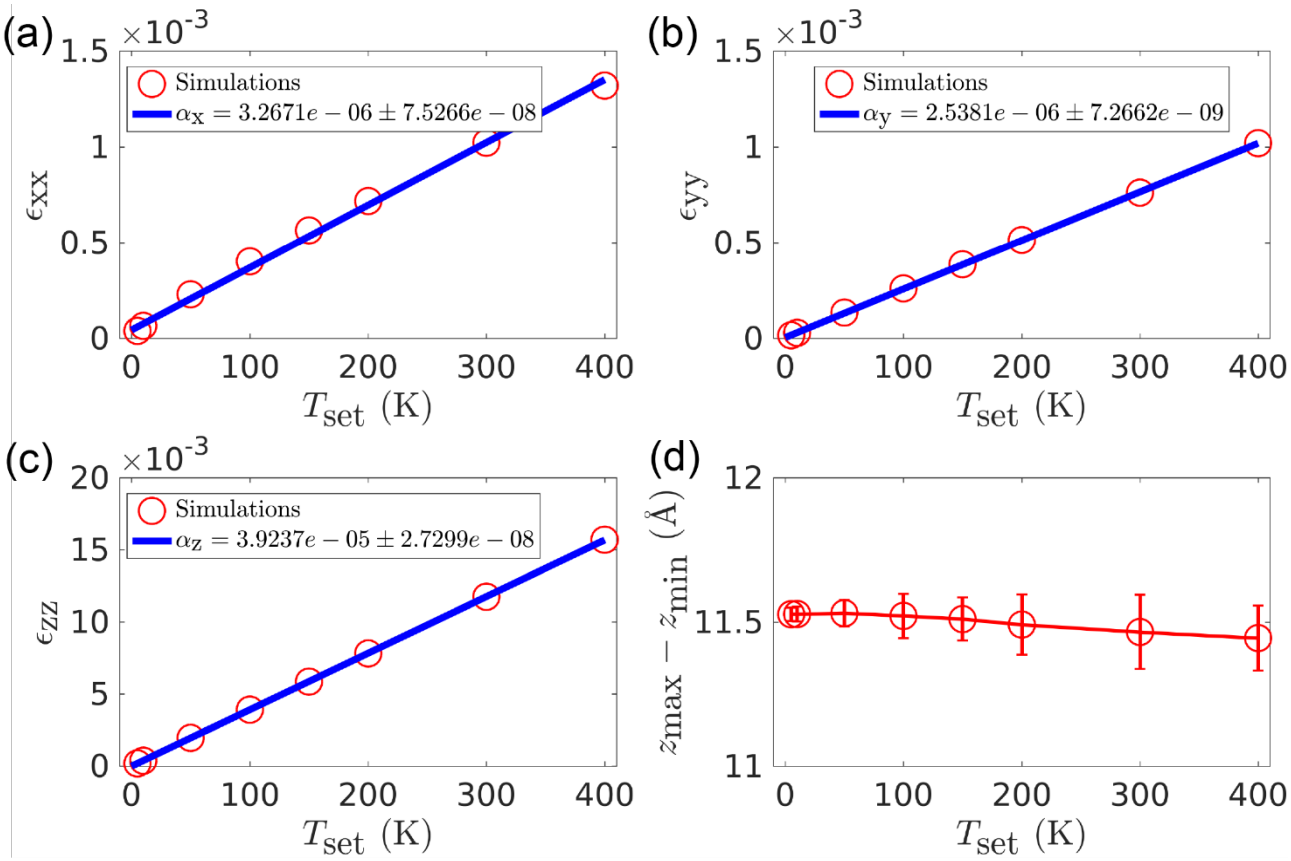

FIG. S14. Thermal expansion of an alternating graphene/*h*-BN bulk heterojunction (three-dimensional periodic boundary conditions with a 12 layers supercell). Panels (a)-(c) show the thermal strain along the lateral (a, b) and vertical (c) directions as a function of temperature (open red circles). The slope of the fitted curve (blue) gives the thermal expansion coefficient in the corresponding directions. Panel (d) shows the maximal (open red circles) and root mean square (open blue squares) out-of-plane corrugation as a function of temperature.

7 Effect of Strain on the Out-of-plane Corrugation of Graphene/*h*-BN Heterostructures

In the main text, we found that the values of Young's modulus for few-layered graphene/*h*-BN heterostructures are much smaller than that of monolayer graphene (~1000 GPa) [16] and *h*-BN (~865 GPa) [17]. We attributed this to the highly corrugated nature of the heterostructures that can flatten upon loading thus reducing in-plane covalent bond elongation effects. To support this point, we calculated the out-of-plane height for various number of layers of graphene/*h*-BN heterostructures as a function of applied strain. As can be seen from Fig. S15, the out-of-plane corrugation (peak-to-dip value) decreases as the applied stain increases, which shows a flattening effect during stretching, as suggested.

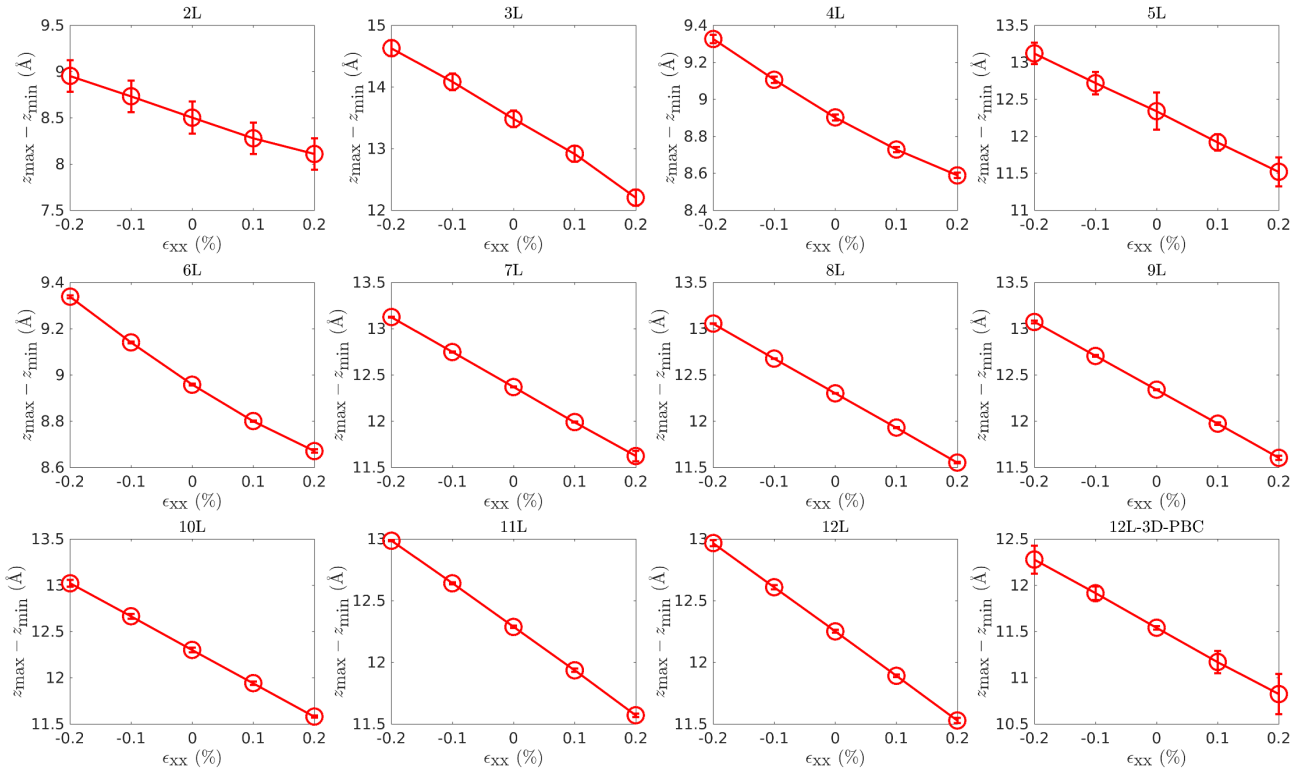

FIG. S15. Out-of-plane corrugation (peak-to-dip value) as a function of the applied strain along the *x*-direction calculated at a temperature of 5 K for alternating graphene/*h*-BN heterostructures with the number of layers varying from 2 to 12. Note that the out-of-plane corrugation is obtained by averaging the peak-to-dip values of all the layers in each heterostructures.

8 Parity-Dependent Superlattices in Alternating Twisted h-BN Heterostructures

In the main text, we stated that the parity dependence of the out-of-plane deformation patterns observed for graphene/*h*-BN heterostructure is attributed to the interplay between the large-scale moiré superlattices formed at each interface in the heterostructures. Based on this we concluded that the parity dependence should be observed in other layered structures possessing large-scale moiré superlattices between adjacent layers and that such structures can be obtained also for homogeneous layered material stacks provided that adjacent layers are placed in a misaligned configuration. To support this conclusion, we presented in the main text results for few-layered alternating homogeneous graphene heterostructures. To further demonstrate the generality of our results we repeated our calculations for few-layered homogeneous alternating stacks of twisted *h*-BN, where every even numbered layer is rotated by 1.12° with respect to its adjacent odd numbered layers (the method for building laterally periodic twisted multilayer graphene and *h*-BN structures can be found in Ref. [15]). The optimized structures for 2-7 layered twisted *h*-BN stacks are presented in Fig. S16. The parity dependence is clearly observed for smaller number of layers and disappears above a thickness of 6 layers, consistent with the results obtained for alternating graphene/*h*-BN heterostructures and homogeneous twisted graphene stacks.

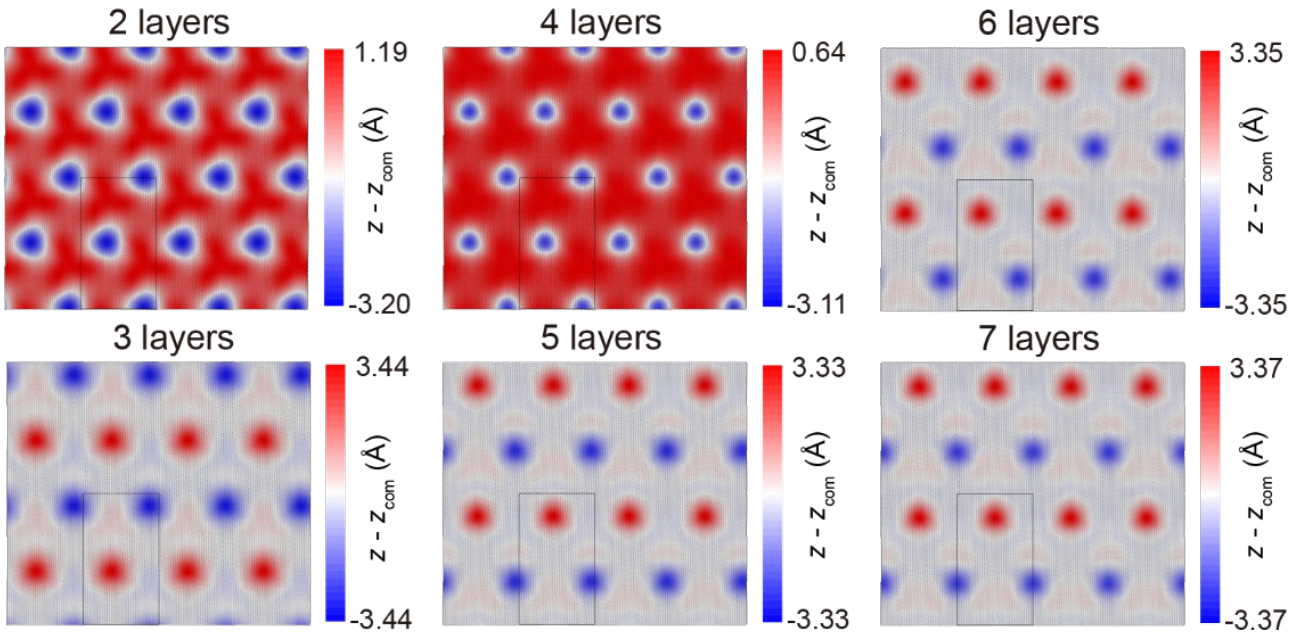

FIG. S16. The out-of-plane deformation pattern for alternating twisted *h*-BN heterostructures. Each even numbered layer is rotated by 1.12° with respect to its adjacent odd numbered layers. To show the deformation pattern clearly, the simulation box (marked by black rectangle in each panel) is multiplied in the lateral directions. The color scales denote the perpendicular height of the top layer atoms with respect to its center-of-mass.

References

[1] Y. Song, D. Mandelli, O. Hod, M. Urbakh, M. Ma, and Q. Zheng, *Robust microscale superlubricity in graphite/hexagonal boron nitride layered heterojunctions*, Nat. Mater. **17**, 894 (2018).

[2] D. Mandelli, W. Ouyang, M. Urbakh, and O. Hod, *The Princess and the Nanoscale Pea: Long-Range Penetration of Surface Distortions into Layered Materials Stacks*, ACS Nano **13**, 7603 (2019).

[3] S. Alexander, *Visualization and analysis of atomistic simulation data with OVITO–the Open Visualization Tool*, Model. Simul. Mater. Sc **18**, 015012 (2010).

[4] D. W. Brenner, O. A. Shenderova, J. A. Harrison, S. J. Stuart, B. Ni, and S. B. Sinnott, *A second-generation reactive empirical bond order (REBO) potential energy expression for hydrocarbons*, J. Phys.: Condens. Matter **14**, 783 (2002).

[5] A. Kınacı, J. B. Haskins, C. Sevik, and T. Çağın, *Thermal conductivity of BN-C nanostructures*, Phys. Rev. B **86**, 115410 (2012).

[6] I. Leven, T. Maaravi, I. Azuri, L. Kronik, and O. Hod, *Interlayer Potential for Graphene/h-BN Heterostructures*, J. Chem. Theory Comput. **12**, 2896 (2016).

[7] T. Maaravi, I. Leven, I. Azuri, L. Kronik, and O. Hod, *Interlayer Potential for Homogeneous Graphene and Hexagonal Boron Nitride Systems: Reparametrization for Many-Body Dispersion Effects*, J. Phys. Chem. C **121**, 22826 (2017).

[8] W. Ouyang, D. Mandelli, M. Urbakh, and O. Hod, *Nanoserpents: Graphene Nanoribbon Motion on Two-Dimensional Hexagonal Materials*, Nano Lett. **18**, 6009 (2018).

[9] W. Ouyang, I. Azuri, D. Mandelli, A. Tkatchenko, L. Kronik, M. Urbakh, and O. Hod, *Mechanical and Tribological Properties of Layered Materials under High Pressure: Assessing the Importance of Many-Body Dispersion Effects*, J. Chem. Theory Comput. **16**, 666 (2020).

[10] S. Plimpton, *Fast Parallel Algorithms for Short-Range Molecular Dynamics*, J. Comput. Phys. **117**, 1 (1995).

[11] W. Shinoda, M. Shiga, and M. Mikami, *Rapid estimation of elastic constants by molecular dynamics simulation under constant stress*, Phys. Rev. B **69**, 134103 (2004).

[12] E. Bitzek, P. Koskinen, F. Gähler, M. Moseler, and P. Gumbsch, *Structural Relaxation Made Simple*, Phys. Rev. Lett. **97**, 170201 (2006).

[13] G. Henkelman and H. Jónsson, *Improved tangent estimate in the nudged elastic band method for finding minimum energy paths and saddle points*, J. Chem. Phys. **113**, 9978 (2000).

[14] G. Henkelman, B. P. Uberuaga, and H. Jónsson, *A climbing image nudged elastic band method for finding saddle points and minimum energy paths*, J. Chem. Phys. **113**, 9901 (2000).

[15] W. Ouyang, H. Qin, M. Urbakh, and O. Hod, *Controllable Thermal Conductivity in Twisted Homogeneous Interfaces of Graphene and Hexagonal Boron Nitride*, Nano Lett. **20**, 7513 (2020).

[16] C. Lee, X. Wei, J. W. Kysar, and J. Hone, *Measurement of the Elastic Properties and Intrinsic Strength of Monolayer Graphene*, Science **321**, 385 (2008).

[17] A. Falin *et al.*, *Mechanical properties of atomically thin boron nitride and the role of interlayer interactions*, Nat. commun. **8**, 15815 (2017).